A case study of connection between ground magnetic field perturbations and tail current sheet bursty flows at X = –60 R_E

Chih-Ping Wang[1], Xiaoyan Xing[2], Yi-Hsin Liu[3], Andrei Runov[4]

1. Department of Atmospheric and Oceanic Sciences, University of California, Los Angeles, California, USA
2. XS Research LLC, Irvine, California, USA
3. Department of Physics and Astronomy, Dartmouth College, Hanover, New Hampshire, USA
4. Department of Earth, Planetary, and Space Sciences, University of California, Los Angeles, California, USA

Abstract. We report the first observations that connect a burst of fast flows and Pi2 fluctuations in the mid-tail current sheet at $X \sim -60\ R_E$ with ground magnetic negative bays and Pi2 pulsations at high-latitudes near 70^o. Both the flow burst and negative bays occurred around midnight and were isolated and lasted for ~10 min. The flow burst had the characteristics of a low-density plasma bubble. It was moving earthward at ~340 km/s and was accompanied by field-aligned currents. The timing and equatorward motion of magnetic bays can be accounted for by this earthward moving bubble. Enhanced Pi2 fluctuations were observed within both the bubble and the magnetic bays. Pressure anisotropy with higher parallel pressure was observed associated with the flow burst and was firehose unstable. We discuss firehose instability as one of the possible mechanisms for the Pi2 fluctuations.

1. Introduction

Nightside ionosphere at auroral latitudes is magnetically connected to the magnetotail current sheet. Major magnetic field disturbances observed on the ground, such as magnetic bays and Pi2 pulsations (6-25 mHz and 40–150 s), have been associated with different disturbances in the tail. Magnetic bays have been observed during substorms, pseudo-breakups, or poleward boundary intensifications [*Lyons et al*., 1999]. They are often associated with bursty bulk flows (BBFs) and magnetic field dipolarization in the tail plasma sheet, during which the connection between the currents in the ionosphere and tail is established through a substorm current wedge (SWC) current system [e.g., *McPherron*, 1972; *Kepko et al*., 2015]. Pi2 pulsations can be observed either during quiet times or disturbed times [e.g., *Keiling and Takahashi*, 2011]. Ground Pi2 pulsations at high latitudes have been observed within an interval of magnetic bays [*Keiling et al*., 2008; *Murphy et al.*, 2011]. BBFs have been considered as one of many different energy sources for Pi2 pulsations. Many observational studies have shown space Pi2 pulsations associated with BBFs [e.g, *Saito et al.*, 2008; *Xing et al*., 2015], as well their connections with ground Pi2 pulsations [e.g., *Kepko and Kivelson*, 1999, *Murphy et al*., 2011; *Runov et al*., 2014, *Gabrielse et al*., 2017]. *Kepko and Kivelson* [1999] correlated BBF velocity variations with ground Pi2 waveforms. *Gabrielse et al*. [2017] showed that ground Pi2 pulsations were observed earlier at higher latitudes, in good correspondence with earthward moving BBFs. However, the satellite data used in these previous studies were at $r < \sim 20\ R_E$, so they may only observe BBFs that were likely propagated from further down the tail. It thus remains unclear whether high-latitude Pi2 pulsations are connected to BBFs in near-Earth ($r < \sim 30\ R_E$), mid-tail (r ~30-100 R_E), or distant tail ($r > 100\ R_E$) current sheet. In this paper, using simultaneous observations from ground magnetometers and Acceleration Reconnection Turbulence and Electrodynamics of

59 Moon's Interaction with the Sun (ARTEMIS) in the tail, we present a case study showing that
60 ground magnetic bays and Pi2 pulsation observed at ~70^{o} latitude were very likely connected to
61 mid-tail BBFs observed at $X \sim -60\ R_E$. This is, to our knowledge, the first observational study to
62 establish such magnetic connection between the ionosphere and mid-tail current sheet. We select
63 this particular event because of many good circumstance conditions. The tail current sheet had
64 been relatively steady for more than 1 hr. Both ARTEMIS and ground magnetometers were close
65 to midnight. The perturbations observed at both ARTEMIS and ground were sharp and isolated.
66 The two ARTEMIS probes were separated in the X direction and the ground magnetometers
67 were aligned along approximately the same geomagnetic longitudes, which were ideal for
68 determination of earthward and equatorward propagation of the disturbances. These good
69 conditions allow for establishing the tail-ionosphere connection with less ambiguity. Such
70 ground-ARTEMIS conjunction events were very rare and the conditions were the most ideal for
71 this event. We present the ARTEMIS observations of the BBFs in section 2. Magnetic bays
72 observed on the ground and their connection with the BBFs were presented in section 3. The Pi2
73 pulsations observed in both the tail and on the ground were presented in section 4. In section 5
74 we discuss firehose instability as one of possible mechanisms for generating the Pi2 fluctuations
75 in the tail by comparing the results of a PIC simulation with ARTEMIS observations.

76 **2. BBFs and Plasma Bubble in Mid-Tail**

77 In this event study, a burst of mid-tail BBFs was observed by the two ARTEMIS probes
78 [*Sibeck et al*., 2011], P1 and P2, at ~05:25 UT on 6 December 2014 at $X \sim -60\ R_E$. ARTEMIS
79 magnetic field vectors (3 s resolution) were measured by the fluxgate magnetometer (FGM)
80 instrument [*Auster et al*., 2008], and plasma moments (3 s resolution) were measured by the
81 electrostatic analyzer (ESA, 0.006–20 keV/q for ions and 0.007–26 keV for electrons)

82 [*McFadden et al*., 2008] and the solid state telescope (SST, 35 keV–6 MeV for ions and 30 keV–
83 6 MeV for electrons). Figures 1a shows observations of P1 (in blue) and P2 (in red) from 05:10
84 to 05:50 UT. Prior to 05:25 UT, both probes were in the plasma sheet (as indicated by hot ions of
85 ~2 keV and small magnetic field strengths) and observed only weak and gradual plasma and
86 magnetic field variations with bulk flow speed less than ~100 km/s. This relatively quiet plasma
87 sheet had lasted for more than one hour since ~04:10 UT. At ~05:25 UT, bulk flows were
88 sharply enhanced in the earthward direction; it reached ~600 km/s but the enhancement quickly
89 diminished at ~05:36 UT. Within this 11 min flow burst, density and pressure dropped
90 significantly by a factor of ~2, while temperature increased by a factor of ~1.5. This density
91 reduction indicated that this flow burst was associated with a plasma bubble. Magnetic fields
92 also changed significantly within the plasma bubble with magnetic field strength jumping to ~13
93 nT. The quiet plasma sheet beforehand and the isolated flow burst allowed for identifying the
94 initiation and duration of the tail disturbances, as well as corresponding ground disturbances,
95 with less timing ambiguity.

96 There was a slight difference between the times when the two probes observed the bubble,
97 suggesting the bubble was propagating. However, in this case the observed peak bulk flow speed
98 cannot be used to represent the propagation speed. Within the bubble, electric drift ($V_{E\times B}$), as
99 shown in Figure 1a, was substantially smaller than bulk flows. The difference at the flow peak at
100 ~05:27 UT was due to strong diamagnetic drift resulting from sharp plasma and magnetic field
101 gradients, while the difference after the flow peak is to the parallel flows. Diamagnetic drift
102 includes a magnetization component not associated with transport, thus making it unreliable to
103 use bulk speeds for the bubble's propagation speeds. Figure 1b shows the probe locations in
104 aberrated geocentric solar magnetospheric coordinates (A-GSM, the aberration angle was ~4^o

105 corresponding to the solar wind speed of ~400 km/s at the time [e.g., *Dmitriev et al.*, 2003]). At
106 05:25 UT (as indicated by squares) the two probes were mainly separated in the *X* direction with
107 P1 being ~1.05 R_E earthward of P2 (the separations in the *Y* and *Z* directions were ~0.2 R_E),
108 allowing for estimating the bubble's propagation in the *X* direction. Note that the alignment
109 between the two probes kept changing as the probes moved, so that having such particular
110 alignment right at the beginning of a flow burst was rare. This is an important reason for us to
111 select this event. Figure 1c shows |*B*| observed by P1 from 05:24 to 05:28 UT (in blue). A good
112 match in the sharp *B* increase (dipolarization front) was found with that of P2 (in red) if P2 data
113 were time-shifted forward by 18-21 s (considering the 3 s uncertainty of the *B* measurements),
114 indicating that the bubble was propagating earthward at speeds of ~344±26 km/s. In the previous
115 studies of earthward-moving bubbles in the near-Earth plasma sheet using multiple satellites
116 [e.g., *Runov et al*., 2012], it is found that the propagation speeds inferred from two satellites were
117 close to the average bulk flow speeds within the bubbles. In our event, the bulk flow speeds
118 averaged over 05:25 to 05:36 UT were 340 and 320 km/s for P1 and P2, respectively, which
119 were within the range of the above inferred speeds. If the bubble passed through the probes at a
120 constant propagation speed of 344 km/s, the *X*-scale of the bubble would be ~35 R_E.

121 Figure 2a shows the magnetic field variations and their 5 min running averages (in black)
122 observed by P1 associated with the flow burst from 05:24 to 05:38 UT. Within the bubble, B_x
123 and B_z were enhanced in the positive direction, while there was a bipolar variation in B_y. Such
124 bipolar variations are similar to those observed in a flux transfer events (FTE) along the
125 magnetopause [e.g., *Zhang et al*., 2008], and are likely associated with a helical magnetic
126 structure generated by field-aligned currents (FACs) flowing through a twisted flux tube. In the
127 *Zhang et al*. study, they were able to reproduce the observed FTE magnetic fields with helical

128 magnetic fields generated by the *Kivelson and Khurana* [1995] model. Therefore we also apply
129 this model to fit our observations. To account for the observed B_y bipolar profile and the B_x and
130 B_z enhancements, the model core magnetic field is tilted from the *X*-*Y* plane with a large angle,
131 and the FAC is directed downward to the current sheet (upward from the ionosphere). As shown
132 in Figure 2a, the model fields (in red) are qualitatively consistent with the observed field
133 variations. Despite some quantitative discrepancies in the B_x and B_z enhancements, which is
134 likely due to current sheet motion relative to the satellite, this qualitative agreement is sufficient
135 to indicate the existence of a FAC associated with this flow burst. Figure 2b shows that V_y
136 observed by P2 started to increase in the positive direction ahead of the flow burst, but it turned
137 sharply negative and was enhanced within the burst. Such FAC and V_y profiles are consistent
138 with magnetohyrodyamic simulation results of *Birn et al*. [2004], which predicted the generation
139 of FACs and flow vortices by a moving plasma bubble. The predicted FAC is downward
140 (upward) to the current sheet, and the predicted flow vortex is counterclockwise (clockwise) on
141 the duskside (dawnside) of an earthward-moving bubble; therefore the observed magnetic fields
142 and flows suggest that P1 likely observed the duskward side of the plasma bubble. Figure 2c
143 illustrates these magnetic field and flow perturbations relative to the ARTEMIS probe.

144 **3. Magnetic Bays on the Ground**

145 The FACs inferred from the observed magnetic field perturbations within the plasma bubble
146 shown in Figure 2 are expected to cause transient enhancements in the perpendicular currents
147 flowing in the ionosphere (electrojets) because of current continuity ($\nabla \cdot \mathbf{J} = 0$, where $\mathbf{J}$ is current
148 density). As a result, magnetic field perturbations on the ground are enhanced. Figure 3a shows
149 ground magnetic field perturbations indicated by SML index derived from SuperMAG [*Gjerloev*,
150 2009; 2012]. SML, similar to AL index, indicates the maximum westward auroral electrojets

151 strength. SML is computed from the lower envelope of the north-south component for stations
152 between 40° and 80° magnetic latitudes in the northern hemisphere (typically ~100 stations),
153 while AL is derived only from 12 stations between 60° and 71° magnetic latitudes. So for an
154 electrojet of smaller spatial scale or at latitudes higher or lower than the nominal auroral zone,
155 SML can better catch its ground perturbations than does AL. Figure 3a shows that SML started
156 to decrease from –100 nT at ~05:22 UT and dropped to its minimum of –220 nT at 05:35 UT,
157 but it then increased back to –100 nT at 05:45 UT. This SML enhancement occurred around the
158 time of the mid-tail flow burst, thus supporting their expected connection through the FACs.
159 To further investigate the magnetic connection between the mid-tail and the ionosphere, we
160 estimate ARTEMIS footprint by using the Tsyganenko 96 (T96) magnetic field model
161 [*Tsyganenko et al.*, 1995; 1996]. The T96 model is the only empirical model that is capable of
162 predicting magnetic fields in the mid-tail and beyond. The later versions of Tsyganenko
163 magnetic field models were developed specifically only for storm times and for the region
164 earthward of $X = -15\ R_E$. For the inputs to the T96 model, we use the observed IMF B_y and IMF
165 B_z dynamic pressure (P_{SW}), and SYM-H from OMNI data [*King and Papitashvili*, 2005], as
166 shown in Figures 3b-3d. P_{SW} was about 3.5 nPa with no strong variation (the solar wind density
167 was ~10.5 cm^{-3}) and SYM/H was ~0. IMF B_x and B_y were relatively steady, while IMF B_z was
168 southward from ~04:58 to 05:15 UT and then remained around zero afterward. Note that these
169 IMF and P_{SW} have been shifted to the Earth's bow shock nose, which was at X ~12 R_E at the
170 time. Considering that the solar wind speed was ~400 km/s and it would take another 19 min for
171 these conditions to reach $X = -60\ R_E$, we use the conditions between 05:00 and 05:20 UT to
172 estimate the T96 fields at ARTEMIS locations between 05:20 and 05:40 UT. The T96 lobe fields
173 at $X = -60\ R_E$ were ~11 nT, slightly smaller than the observed lobe field of ~13 nT inferred from

174 total plasma and magnetic pressures, suggesting that the estimates by using the T96 model
175 presented below are likely appropriate for this event. Figure 3e shows the estimated ionosphere
176 footprints of P1 (red triangles), together with mapping of equatorial locations at fixed X and Y
177 (red dotted lines). The footprint of P2 was very close to that of P1, so only the P1 footprint is
178 plotted. The ARTEMIS footprint was at ~69^o to 71^o magnetic latitudes and at ~362^o to 364^o
179 magnetic longitudes (at MLT ~0.6 as midnight at 05:30 UT is indicated by the purple vertical
180 line). Since ARTEMIS was close to midnight, we expect that the MLTs of the field-line mapping
181 should not be significantly affected by IMF B_y penetration into the tail magnetosphere.
182 To investigate magnetic field perturbations on the ground in a good MLT conjunction with
183 ARTEMIS, we first examined all ground magnetometers within ~3 hr MLT from the ARTEMIS
184 footprint and between 65^o to 80^o latitudes. These stations, as plotted in Figure 3e, were mapped
185 to most of the tail from $X \sim -10$ to beyond -100 R_E and $|Y| < \sim 15$ R_E. Figure 3f shows
186 perturbations in the H (in blue) and Z (in red) components at these stations. Note that these
187 stations are plotted in a way that the stations of the same column (row) are at similar magnetic
188 longitudes (latitudes), and the blank panels are also plotted to fill those longitudes and latitudes
189 where there was no station. The ground magnetic field components are defined in the
190 geomagnetic coordinates. H is along the north-south direction (positive is northward), D is along
191 the east-west direction (positive is eastward), and Z is along the vertical direction (positive is
192 downward). The perturbations are computed by subtracting their 30 min running averages. It can
193 be seen that the largest ground perturbations were observed at AKUL station, which was very
194 close to the ARTEMIS footprint at the time. Note that the perturbations at AKUL station was the
195 main contributor to the SML minimum shown in Figure 3a. This mapping thus suggests that the

196 ground perturbations were very likely caused by the FACs associated with the bubble observed
197 at ARTEMIS.

198 AKUL belongs to a chain of stations (CDRT, SALU, PUVR, INUK, and SNKQ) that were
199 aligned approximately along the MLT of the ARTEMIS footprint from ~66^{o} to 74^{o} latitudes.
200 These stations were thus ideal for investigating latitudinal propagation of ground perturbations.
201 Figure 4a shows ground magnetic field perturbations (subtracting their 30 min running averages)
202 in the H (in blue), D (in purple), and Z (in green) components at five of these stations. Magnetic
203 negative bays with sharp drops in H and D for ~10–15 min were observed at almost all stations.
204 The minimum of ΔH (indicated by the blue vertical dotted lines) approximately coincided with
205 the minimum of ΔD, while ΔZ changed signs at the ΔH minimum from pointing upward before
206 to pointing downward after the minimum. The perturbations were seen to occur earlier at stations
207 at higher latitudes. The ΔH minimum occurred at ~74^{o} (CDRT) at ~05:27:30 UT and later at
208 ~69^{o} (PUVR) at ~05:39 UT. At 67.5^{o} (INUK), ΔH was very small but a strong ΔD minimum can
209 still be seen at ~05:42 UT. As illustrated in Figure 4b, these correlations between the
210 perturbations in the three components are consistent with being caused by an equatorward
211 moving electrojet within its currents flowing westward and northward. As the electrojet moved
212 equatorward and passed through a station, one would first observe a negative ΔZ when the
213 electrojet was north of the station, then a negative ΔH and zero ΔZ when the electrojet was just
214 overhead of the station, and finally a positive ΔZ after the electrojet moved to south of the
215 station.

216 Interestingly, the B_x perturbation observed by P1 with 6.5 min delay (in red) was found to
217 match well with the H and D perturbations at AKUL station. This time delay can be due to the
218 propagation of shear Alfvén waves from ARTEMIS to the ionosphere. We estimate Alfvén

speeds and propagation times by using the T96 magnetic fields and by assuming a constant density of 0.08 cm^{-3} (the low density within the plasma bubble as shown in Figure 1b). Figure 4c shows the estimated Alfvén speeds (in blue) and propagation times (in red) as a function of the distances along the magnetic field lines from the ARTEMIS location. It would take ~350-400 s for shear Alfvén waves to travel to the ionosphere from $X = -60\ R_E$, which can explain the observed delay. Figure 4d shows the prediction of the *X*-location of the bubble front as a function of time (blue) assuming a constant earthward speed of 340 km/s, together with the arrival latitudes and times of the shear Alfvén waves (red) coming from the bubble front. The predicted ground equatorward motion is consistent with the observations shown in Figure 4a. Also, the predicted equatorward moving speed is ~0.43°/min, in agreement with the observed speed of ~0.4°/min. The above analysis thus strongly suggests that the equatorward-moving magnetic bays are caused by the FACs associated with the earthward-moving plasma bubble in the mid-tail. Note that this is different from polarward-moving magnetic bays associated with tailward expansion of the current wedge resulting from flow-braking in the near-Earth plasma sheet [e.g., *Birn et al*., 2013].

As shown in Figure 3f, earthward propagation of ground perturbations was also observed at PANG, IQA, and KUUJ stations, which were ~10-15° eastward of the ARTEMIS footprint. However, such earthward propagation was not observed at RANK, FCC, and GILL stations, which were ~20° westward of the ARTEMIS footprint. Note the perturbations at FCC and GILL were shorter (2-5 min) and occurred earlier and were actually moving poleward, so that they were more likely associated with a small perturbation in the near-Earth plasma sheet and not with the mid-tail plasma bubble. This suggests that the mid-tail bubble may extend at least ~5 R_E wide in the *Y* direction. This *Y*-scale is expected, as *Li et al.* [2013] showed statistically from

ARTEMIS observations that plasmoids at $X \sim -60\ R_E$ have a width of 5–10 R_E. In global MHD simulations [e.g., *Wiltberger et al*., 2015], there could be more than one plasma bubble occurring simultaneously across the mid-tail. For this event, from these ground perturbations observed by all the stations mapped to most of the tail, it is likely that the plasma bubble observed by ARTEMIS was the only bubble at the time. In addition, there were positive excursions in ΔH and ΔD before the negative bays. These excursions at AKUL and PUVR are likely not an artificial effect of the filtering process. A possible explanation for the excursions is that they were caused by the eastward electrojet of a region-2 sense FAC system generated ahead of the earthward moving bubble, as shown in the observational studies of the near-Earth bubbles [e.g., *Liu et al*., 2013]. However, such region-2 FACs may be too small or ARTEMIS may not be near them so that the currents are not discernable from the ARTEMIS magnetic fields shown in Figure 2 by using our fitting analysis with the model helical magnetic fields.

4. Pi2 Fluctuations in Space and on the Ground

As shown in Figure 2a, associated with the flow burst, there were strong magnetic field fluctuations in periods of ~1-2 min, which is within the Pi2 range (40-150 s). To analyze magnetic field fluctuations in the magnetosphere, we transformed field components to mean-field aligned (MFA) coordinates. The Z_{MFA} component is in the direction of the background magnetic field determined from 5-min running averages (as shown in black lines in Figure 2a), the Y_{MFA} component is the cross product of the spacecraft's position unit vector and Z_{MFA} and it points azimuthally eastward, and the X_{MFA} component completes the orthogonal right-hand system. Figures 5a and 5b show 40-150 s band-pass time series of parallel and perpendicular magnetic fields, plasma pressure (P), and parallel and perpendicular flow speed, observed by P1 and P2, respectively, from 05:10 to 05:45 UT. Pi2 fluctuations in both magnetic field and plasma

were strongly enhanced starting from ~05:25 UT associated with the flow burst. The magnetic field fluctuations were seen in both the parallel (compressional) and perpendicular direction. Figure 5d shows that perturbations of magnetic pressure (P_B) observed at P2 were out of phase with those of plasma pressure (P_p), indicating slow mode waves. Interestingly, the P_B and P_p observed at P1 as shown in Figure 5c show a mixture of phase difference between their perturbations, indicating coexistence of the slow mode with the fast and intermediate modes. This difference between P1 and P2 suggests that a complex Pi2 wave environment was generated within the bubble.

Figure 6a shows that ground Pi2 perturbations can be seen in both the unfiltered (top) and 40-150s band-passed (bottom) time series of the H component observed at AKUL, and that the Pi2 perturbations were amplified within the magnetic bay (magnetic field data with 0.5 s resolutions for these stations were used). Figure 6b shows 40-150 s band-pass time series of magnetic fields in the *H*, *D*, and *Z* components from 05:10 to 05:45 UT observed at the five stations shown in Figure 4a. At all these stations, Pi2 magnetic field perturbations were strongly enhanced in all the 3 components within the magnetic bays (the vertical purple lines indicate the minimum of ΔH shown in Figure 4a). This thus suggests that the space Pi2 waves may be first generated within the bubble in the tail and then propagated to the ionosphere, resulting in the enhancements of the ground Pi2 waves. However, the dominant periods of ground Pi2 waves and the phase correlations between the 3 components vary slightly with latitudes, which may suggest that the characteristics of Pi2 waves within the bubble likely changed as the bubble was moving earthward and evolving. More observational and simulation studies need be conducted in the future in order to understand the Pi2 wave generation within a plasma bubble and its physical connection with the ground Pi2 waves.

5. Conclusion and Discussion

In this study, by using a midnight conjunction of ARTEMIS probes and ground stations, we present the first observational study showing that BBFs and Pi2 pulsations in the mid-tail current sheet at $X \sim -60\ R_E$ were connected to ground magnetic bays and Pi2 pulsations at ~70^o magnetic latitude. The BBFs were associated with a plasma bubble. The bipolar B_y variations within the bubble suggested a flux rope with downward FACs to the tail (upward from the ionosphere). Such FACs were expected to generate ionosphere electrojets and thus can account for magnetic bay perturbations. Both the BBFs and magnetic bays were isolated and lasted for ~11 min. The magnetic bays were observed a few minutes after BBFs, which can be explained by Alfvén propagation times. The BBFs were propagating earthward, in a good correspondence with the magnetic bays moving toward lower latitudes. Pi2 fluctuations were enhanced within both the BBFs and the magnetic bays. These correlations thus connected the mid-tail disturbances with the high-latitude ground perturbations. It is likely that there was aurora activity associated with this event, however, no all-sky imagers were available at the time. Nevertheless, this event may be associated with polarward boundary intensifications (PBIs) [*De La Beaujardière et al.*, 1994], which is localized auroal brightening around the polar-cap boundary, since previous studies have shown that PBIs have the characteristics of high-latitude negative bays [e.g., *De La Beaujardière et al.*, 1994] and Pi2 waves [e.g., *Sutcliffe and Lyons*, 2002]. In addition, the equatorward propagation of negative bays in this event suggests an association with an auroral streamer, a north-south aligned aruoral form extending equatorward from a PBI. Previous studies have also connected BBFs with PBIs [e.g, *Zesta et al*., 2006] and streamers [e.g., *Sergeev et al*., 1999].

It has been suggested that BBFs associated with an earthward-moving plasma bubble can be generated by reconnection in the magnetotail [*Chen and Wolf*, 1993]. Simulations of

311 reconnection using double-adiabatic magnetohydrodynamic codes [e.g. *Hirabayashi and*
312 *Hoshino*, 2013], hybrid codes [e.g., *Hirabayashi and Hoshino*, 2015], and PIC codes [e.g., *Liu et*
313 *al*., 2012] have shown that reconnection can generate a fast-moving plasma cloud (we refer it to
314 as ejecta) with pressure anisotropy of $P_\perp/P_\parallel < 1$. With such anisotropy, a system becomes
315 firehose unstable when the condition of $C_f = 1 - 0.5\cdot(\beta_\parallel - \beta_\perp) < 0$ is satisfied, where $\beta = 2\mu_0 P/B^2$.
316 It has been suggested from simulations that firehose instability can be a mechanism for ULF
317 waves, including Pi2 pulsations [e.g., *Horton et al*., 2004]. Other mechanisms proposed for Pi2
318 pulsations include substorm current wedge, periodic flow bursts, periodic reconnection bursts,
319 and other instabilities such as ballooning instability [*Keiling and Takahashi*, 2011]. In the 2-D
320 PIC simulations of *Liu et al*. [2012], they investigated the reconnection exhaust tailward of the
321 ejecta and found that the region near the current sheet center is firehose unstable. Their analysis,
322 however, did not include the region within the ejecta. We analyze their simulation results for the
323 firehose condition within the ejecta in Figures 7a and 7b. Figure 7a shows fast flows associated
324 with the ejecta (moving toward larger X) generated by quasi-steady reconnection located at $X = 0$
325 (here the PIC results are shown in coordinates similar to GSM but with units in the proton
326 inertial length). The proton inertial length is 0.113 R_E in this simulation and the X-scale of the
327 ejecta is ~6 R_E. Figure 7b shows B_x, plasma parallel pressure ($P_\parallel$, in red) and perpendicular
328 plasma pressure ($P_\perp$, in blue), and C_f as a function of the Z direction across the central part of the
329 ejecta (indicated by the dashed white line in Figure 7a). $P_\perp$ is smaller than $P_\parallel$ inside the ejecta,
330 and the $C_f < 0$ condition is satisfied within a thin region close to the current sheet center where β
331 is high. We compare the simulation results with ARTEMIS observations. Figure 7c shows B_x,
332 plasma pressure, pressure anisotropy, plasma beta, and C_f observed by P2. Around the flow
333 burst, $P_\parallel$ became increasingly larger than $P_\perp$, and $C_f < 0$ was observed when P2 crossed the

region of small B_x (< ~3 nT) and large β (> ~20) (indicated by the vertical black dashed lines). C_f < 0 was also observed by P1 (not shown). Note that P2 did remain close to the current sheet center during the flow burst probably because of the vertical motion of current sheet. This qualitative consistency with the PIC simulation results suggests that firehose instability can be one of the possible mechanisms for the observed Pi2 fluctuations. It thus requires more realistic PIC simulations and more ARTEMIS observations in future studies to further investigate this mechanism. The previous study showed that firehose instability is rare within the BBFs observed in the near-Earth tail [e.g., *Kim et al*., 2010]. But several ARTEMIS event studies in mid-tail have shown firehose instability associated with fast flows [e.g., *Vörös*, 2011; *Hietala et al*., 2015]. It thus requires statistical studies to determine the occurrence rates of firehose instability within the mid-tail BBFs.

Acknowledgement

We thank Vassilis Angelopoulos and Elena Grigorenko for discussion. Chih-PingWang and Xiaoyan Xing are supported by NASA NNX16AJ83G. Yi-Hsin Liu is supported by NASA NNX16AG75G and simulations performed with NERSC Advanced Supercomputing. ARTEMIS data are available for free with the Space Physics Environment Data Analysis System (SPEDAS) software (http://themis.igpp.ucla.edu/software. shtml). We acknowledge NASA NAS5-02099 for ARTEMIS, and C. W. Carlson and J. P. McFadden for ESA data, K. H. Glassmeier, U. Auster and W. Baumjohann for FGM data provided under DLR 50-OC-0302.; J. H. King, N. Papatashvilli at AdnetSystems, NASA GSFC and CDAWeb (https://cdaweb.gsfc.nasa.gov/cdaweb/istp_public/) for OMNI data; M. J. Engebretson and the rest of the MACCS team (MACCS is operated by Augsburg College and funded by the U.S. National Science Foundation and is available for free on

http://space.augsburg.edu/maccs/browsegraphs.html); and Martin Connors and C.T. Russell and the rest of the AUTUMN/AUTUMNX team for GMAG data (http://autumn.athabascau.ca/).

References

Auster, H.U., Glassmeier, K.H., Magnes, W., Aydogar, O., Constantinescu, D., Fischer, D., Fornacon, K.H., Georgescu, E., Harvey, P., Hillenmaier, O., Kroth, R., Ludlam, M., Narita, Y., Okrafka, K., Plaschke, F., Richter, I., Schwarzi, H., Stoll, B., Valavanoglu, A., and Wiedemann, M. (2008), The THEMIS fluxgate magnetometer, Space Sci. Rev., doi: 10.1007/s11214-008-9365-9.

Birn, J., J. Raeder, Y. L. Wang, R. A. Wolf, and M. Hesse (2004b), On the propagation of bubbles in the geomagnetic tail, Ann. Geophys., 22, 1773– 1786.

Birn, J., and M. Hesse (2013), The substorm current wedge in MHD simulations, J. Geophys. Res. Space Physics, 118, 3364–3376, doi:10.1002/jgra.50187.

Chen, C. X., and R. A. Wolf (1993), Interpretation of high‐speed flows in the plasma sheet, J. Geophys. Res., 98(A12), 21,409–21,419, doi:10.1029/93JA02080.

De la Beaujardie`re, O., et al., Quiet-time intensifications along the poleward auroral boundary near midnight, J. Geophys. Res., 99, 287–298, 1994.

Dmitriev, A. V., J. K. Chao, and D. J. Wu (2003), Comparative study of bow shock models using Wind and Geotail observations, J. Geophys. Res., 108, 1464, doi:10.1029/2003JA010027, A12.

Gabrielse, C., V. Angelopoulos, C. Harris, A. Artemyev, L. Kepko, and A. Runov (2017), Extensive electron transport and energization via multiple, localized dipolarizing flux bundles, J. Geophys. Res. Space Physics, 122, doi:10.1002/ 2017JA023981.

Gjerloev, J. W. (2009), A Global Ground-Based Magnetometer Initiative, EOS, 90, 230-231,

doi:10.1029/2009EO270002.

Gjerloev, J. W. (2012), The SuperMAG data processing technique, J. Geophys. Res., 117, A09213, doi:10.1029/2012JA017683.

Hietala, H., J. F. Drake, T. D. Phan, J. P. Eastwood, and J. P. McFadden (2015), Ion temperature anisotropy across a magnetotail reconnection jet, *Geophys. Res. Lett.*, *42*, 7239–7247, doi:10.1002/2015GL065168.

Hirabayashi, K., *and* M. Hoshino (2013), Magnetic reconnection under anisotropic magnetohydrodynamic approximation, Phys. Plasmas, 20(11, 112111), doi:10.1063/1.4831754.

Higashimori, K., *and* M. Hoshino (2015), Ion beta dependence on the development of Alfvénic fluctuations in reconnection jets, J. Geophys. Res. Space Physics, 120, 1803–1813, doi:10.1002/2014JA020544.

Horton, W., B.-Y. Xu, and H. V. Wong (2004), Firehose driven magnetic fluctuations in the magnetosphere, Geophys. Res. Lett., 31, L06807, doi:10.1029/2003GL018309.

Keiling, A. and K. Takahashi (2011), Review of Pi2 Models, Space Sci Rev, 161:63-148, doi: 10.1007/s11214-011-9118-4.

Keiling, A., et al. (2008), Periodic traveling compression regions during quiet geomagnetic conditions and their association with ground Pi2, Ann. Geophys., 26, 3341–3354, *doi:*10.5194/angeo-26-3341-2008.

Kepko, L., and M. Kivelson (1999), Generation of Pi2 pulsations by bursty bulk flows, J. Geophys. Res., 104(A11), 25021–25034, doi:10.1029/1999JA900361.

King, J. H., and N. E. Papitashvili (2005), Solar wind spatial scales in and comparisons of hourly Wind and ACE plasma and magnetic field data, J. Geophys. Res., 110, A02104,

403 doi:10.1029/2004JA010649.
404 Kivelson, M. G., and K. K. Khurana (1995), Models of flux ropes embedded in a harris neutral
405 sheet: Force-free solutions in low and high beta plasmas, J. Geophys. Res., 100(A12),
406 23637–23645, doi:10.1029/95JA01548.
407 Li, S.-S., V. Angelopoulos, A. Runov, and S. A. Kiehas (2014), Azimuthal extent and properties
408 of midtail plasmoids from two-point ARTEMIS observations at the Earth-Moon Lagrange
409 points, J. Geophys. Res. Space Physics, 119, 1781–1796, doi:10.1002/2013JA019292.
410 Liu, Y-H., J. F. Drake, and M. Swisdak (2012), The structure of the magnetic reconnection
411 exhaust boundary, Phys. Plasmas, 19(2), 022110, doi:10.1063/1.3685755.
412 Liu, J., V. Angelopoulos, A. Runov, and X.-Z. Zhou (2013), On the current sheets surrounding
413 dipolarizing flux bundles in the magnetotail: The case for wedgelets, J. Geophys. Res.
414 Space Physics, 118, 2000–2020, doi: 10.1002/jgra.50092.

415 Lyons, L. R., T. Nagai, G. T. Blanchard, J. C. Samson, T. Yamamoto, T. Mukai, A. Nishida, *and*
416 S. Kokubun (1999), Association between Geotail plasma flows and auroral poleward
417 boundary intensifications observed by CANOPUS photometers, J. Geophys. Res.,
418 104(A3), 4485–4500, doi:10.1029/1998JA900140.
419 McFadden, J. P., Carlson, C. W., Larson, D., Angelopoulos, V., Ludlam, M., Abiad, R., Elliott,
420 B., Turin, P., Marckwordt, M. (2008), The THEMIS ESA plasma instrument and in-flight
421 calibration, Space Sci. Rev, doi: 10.1007/s11214-008-9440-2.
422 McPherron RL (1972) Substorm related changes in the geomagnetic tail: the growth phase.
423 Planet Space Sci 20(9):1521–1539
424 Murphy, K. R., I. J. Rae, I. R. Mann, A. P. Walsh, D. K. Milling, *and* A. Kale (2011), The
425 dependence of Pi2 waveforms on periodic velocity enhancements within bursty bulk

426 flows, Ann. Geophys., 29(3), 493–509, doi:10.5194/angeo-29-493-2011.
427 Runov, A., V. Angelopoulos, and X.-Z. Zhou (2012), Multipoint observations of dipolarization
428 front formation by magnetotail reconnection, J. Geophys. Res., 117, A05230,
429 doi:10.1029/2011JA017361.

430 Runov, A., V. A. Sergeev, V. Angelopoulos, K.-H. Glassmeier, and H. J. Singer (2014),
431 Diamagnetic oscillations ahead of stopped dipolarization fronts, J. Geophys. Res. Space
432 Physics, 119, 1643–1657, doi:10.1002/2013JA019384.
433 Saito, M. H., Y. Miyashita, M. Fujimoto, I. Shinohara, Y. Saito, and T. Mukai (2008), Modes
434 and characteristics of low-frequency MHD waves in the near-Earth magnetotail prior to
435 dipolarization: Fitting method, J. Geophys. Res., 113, A06201,
436 doi:10.1029/2007JA012778.
437 Sergeev, V. A., K. Liou, C.-I Meng, P. T. Newell, M. Brittnacher, G. Parks, and G. D. Reeves,
438 Development of auroral streamers in association with impulsive injections to the inner
439 magnetotail, Geophys. Res. Lett., 26, 417–420, 1999.

440 Sibeck, D. G., et al. (2011), ARTEMIS science objectives, Space Sci. Rev., 165, 59–91,
441 doi:10.1007/s11214-011-9777-9.

442 Sutcliffe, P. R., and L. R. Lyons (2002), Association between quiet-time Pi2 pulsations,
443 poleward boundary intensifications, and plasma sheet particle fluxes, Geophys. Res. Lett.,
444 29(9), doi:10.1029/2001GL014430.

445 Tsyganenko, N. A.,
446 Modeling the Earth's magnetospheric magnetic field confined within a realistic magnetopause, J.
447 Geophys. Res., 100, 5599– 5612, 1995.
448 Tsyganenko, N. A., Effects of the solar wind conditions on the global magnetospheric
449 configuration as deduced from data-based field models, in Proceedings of the ICS-3

Conference on Substorms, Eur. Space Agency Spec. Publ. 389, pp. 181 – 185, Eur. Space Agency, Noordwijk, Nether- lands, 1996.

Vörös, Z. (2011), Magnetic reconnection associated fluctuations in the deep magnetotail: ARTEMIS results, Nonlin. Processes Geopphys., 18, 861-869, doi:10.5194/npg-18-861-2011.

Wiltberger, M., V. Merkin, J. G. Lyon, and S. Ohtani (2015), High-resolution global magnetohydrodynamic simulation of bursty bulk flows, *J. Geophys. Res. Space Physics*, *120*, 4555–4566, doi:10.1002/2015JA021080.

Xing, X., C.-P. Wang, J. Liang, and L. R. Lyons (2015), Plasma sheet Pi2 pulsations associated with bursty bulk flows, J. Geophys. Res. Space Physics, 120, 8692–8706, doi:10.1002/2015JA021668.

Zesta, E., L. Lyons, C.-P. Wang, E. Donovan, H. Frey, and T. Nagai (2006), Auroral poleward boundary intensifications (PBIs): Their two-dimensional structure and associated dynamics in the plasma sheet, J. Geophys. Res., 111, A05201, doi:10.1029/2004JA010640.

Zhang, H., K. K. Khurana, M. G. Kivelson, V. Angelopoulos, Z. Y. Pu, Q.-G. Zong, J. Liu, and X.-Z. Zhou (2008), Modeling a force-free flux transfer event probed by multiple Time History of Events and Macroscale Interactions during Substorms (THEMIS) spacecraft, J. Geophys. Res., 113, A00C05, doi:10.1029/2008JA013451.

Captions

Figure 1. (a) Bulk velocity, ion density, ion pressure, ion temperature, magnetic field strength, and $V_{E\times B}$ observed by P1 and P2. (b) *X*-*Y* and *X*-*Z* projections of P1 and P2 trajectories from 05:10 to 05:50 UT (squares indicate the locations at 05:25 UT). (c) $|B|$ observed by P1 (blue) and P2. P2 was time shifted forward by 18 (green) and 21s (red).

Figure 2. (a) Magnetic field components observed by P1. The black lines indicated 3 min averages and red lines are magnetic fields of the flux rope model. (b) Velocity components observed by P1. (c) Illustration of the likely magnetic field and velocity distributions projected on the *X*-*Y* plane based on P2 observations.

Figure 3. (a) SML index, (b) IMF, (c) the solar wind dynamic pressure, and (d) SYM-H. (e) Magnetic longitudes and latitudes of ground stations (blue triangles) and footprint of P1 (red triangles). The red dotted lines indicate the mapping of equatorial locations at fixed *X* and *Y*. (f) Perturbations of the H (blue) and Z (red) components on the ground. The two numbers inside the parentheses indicate magnetic longitude and latitude.

Figure 4. (a) Perturbations of the H, D, Z components of ground magnetometers. (b) Illustrations of ionosphere electrojet $J_{\perp}$ (the blue arrows) and the associated ground perturbations (the red arrows). (c) Alfvén speeds and travel times as a function of field-aligned distances. (d) Predicted X-locations of the bubble front (blue) and ground arrival latitudes of FACs from the bubble front as a function of time.

Figure 5. 40–150 s band-passed fluctuations of parallel and perpendicular magnetic field, plasma pressure, and parallel and perpendicular speed observed by (a) P1 and (b) P2. 40-150 s band-passed fluctuations of magnetic pressure (P_B) and plasma pressure (P_p) observed by (c) P1 and (d) P2.

Figure 6. (a) Unfiltered (top) and 40-150 s band-passed H component at AKUL. (b) 40–150 s band-passed H, D, and Z components at different stations (the purple vertical lines indicate the ΔH minimum).

Figure 7. (a) Simulated V_x/V_A on the X-Z plane. V_A is Alfvén speed. (b) Simulated B_x, parallel and perpendicular plasma pressures, and C_f as a function of Z at $X = 100$. B_0 and P_0 are the initial values at the lobe ($Z = 5$). (c) B_x, plasma pressure, pressure anisotropy, plasma beta, and C_f observed by P1. The vertical black dashed lines indicate where $C_f < 0$.

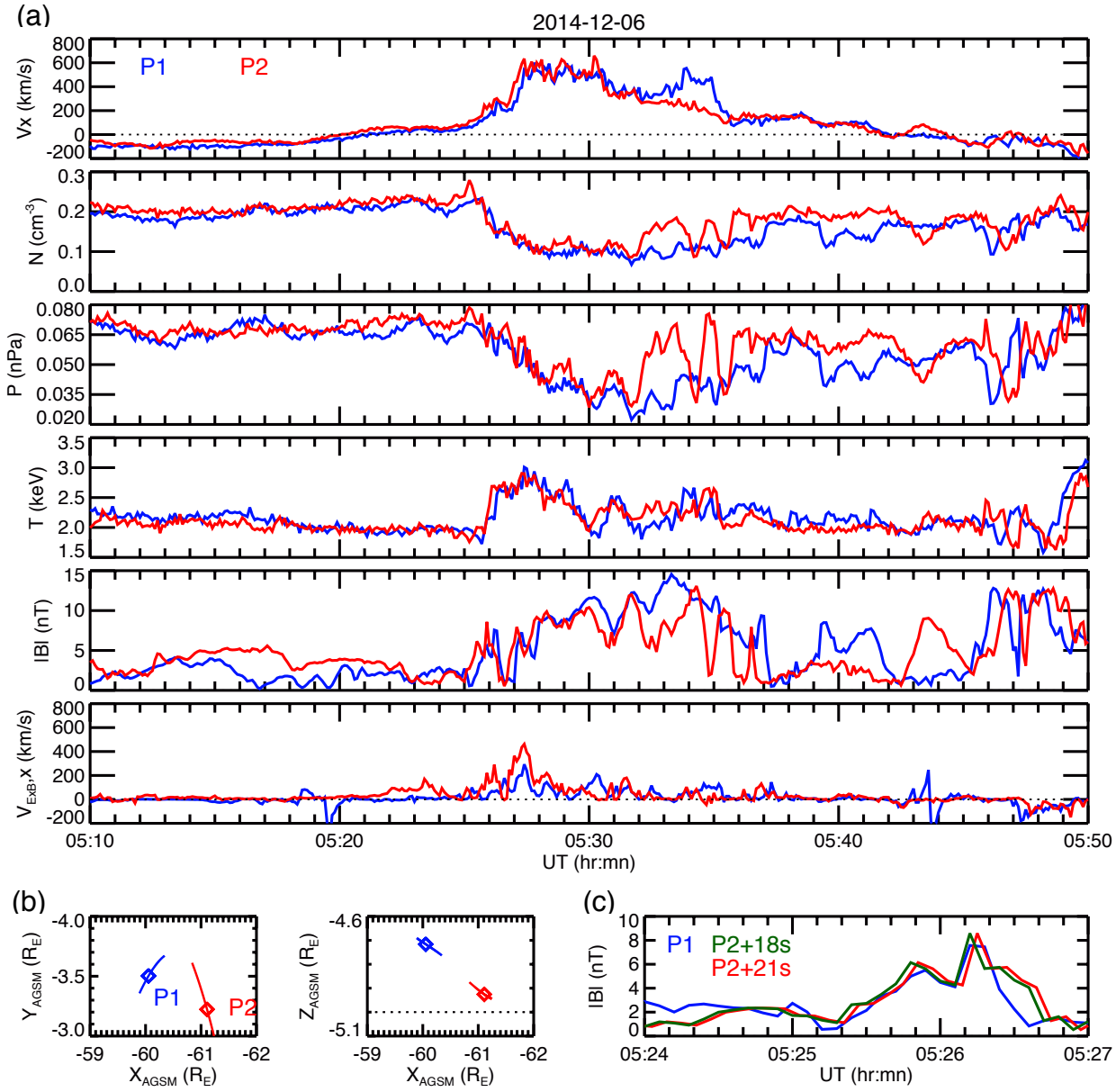

Figure 1.(a) Bulk velocity, ion density, ion pressure, ion temperature, magnetic field strength, and $V_{E\times B}$ observed by P1 and P2. (b) X-Y and X-Z projections of P1 and P2 trajectories from 05:10 to 05:50 UT (squares indicate the locations at 05:25 UT). (c) |B| observed by P1 (blue) and P2. P2 was time shifted forward by 18 (green) and 21s (red).

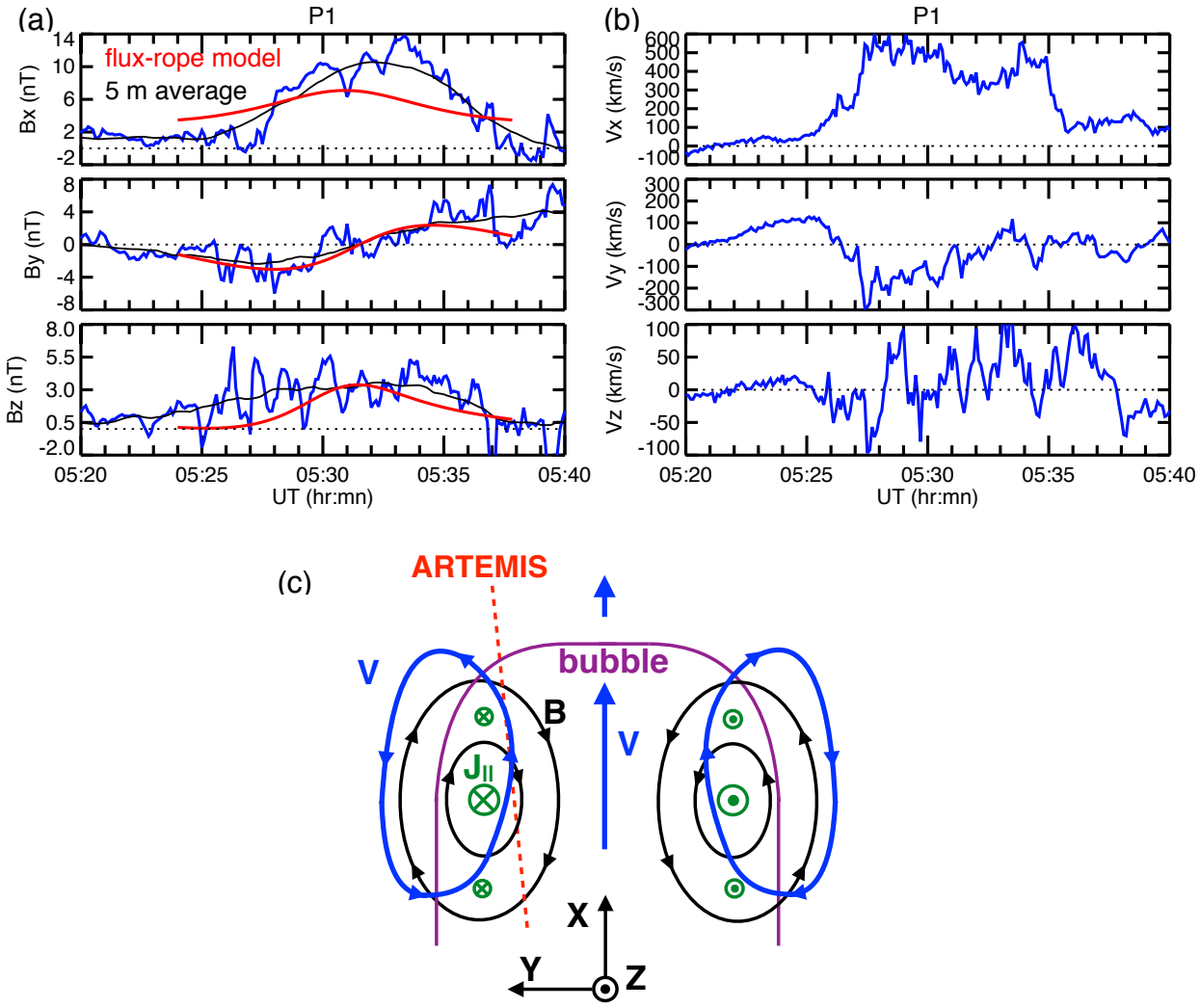

Figure 2. (a) Magnetic field components observed by P1. The black lines indicated 3 min averages and red lines are magnetic fields of the flux rope model. (b) Velocity components observed by P1. (c) Illustration of the likely magnetic field and velocity distributions projected on the X-Y plane based on P2 observations.

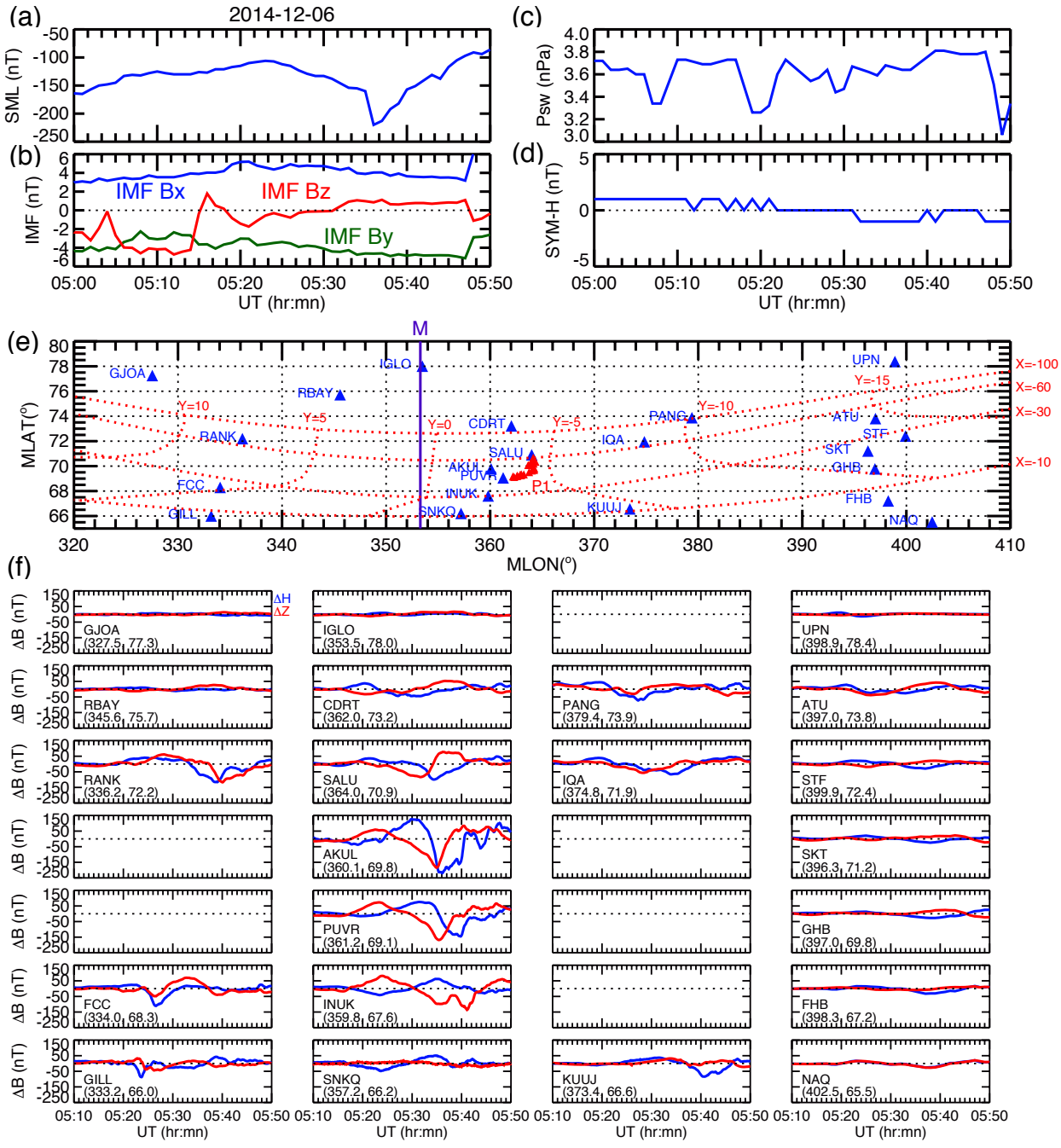

Figure 3. (a) SML index, (b) IMF, (c) the solar wind dynamic pressure, and (d) SYM-H. (e) Magnetic longitudes and latitudes of ground stations (blue triangles) and footprint of P1 (red triangles). The red dotted lines indicate the mapping of equatorial locations at fixed *X* and *Y*. (f) Perturbations of the H (blue) and Z (red) components on the ground. The two numbers inside the parentheses indicate magnetic longitude and latitude.

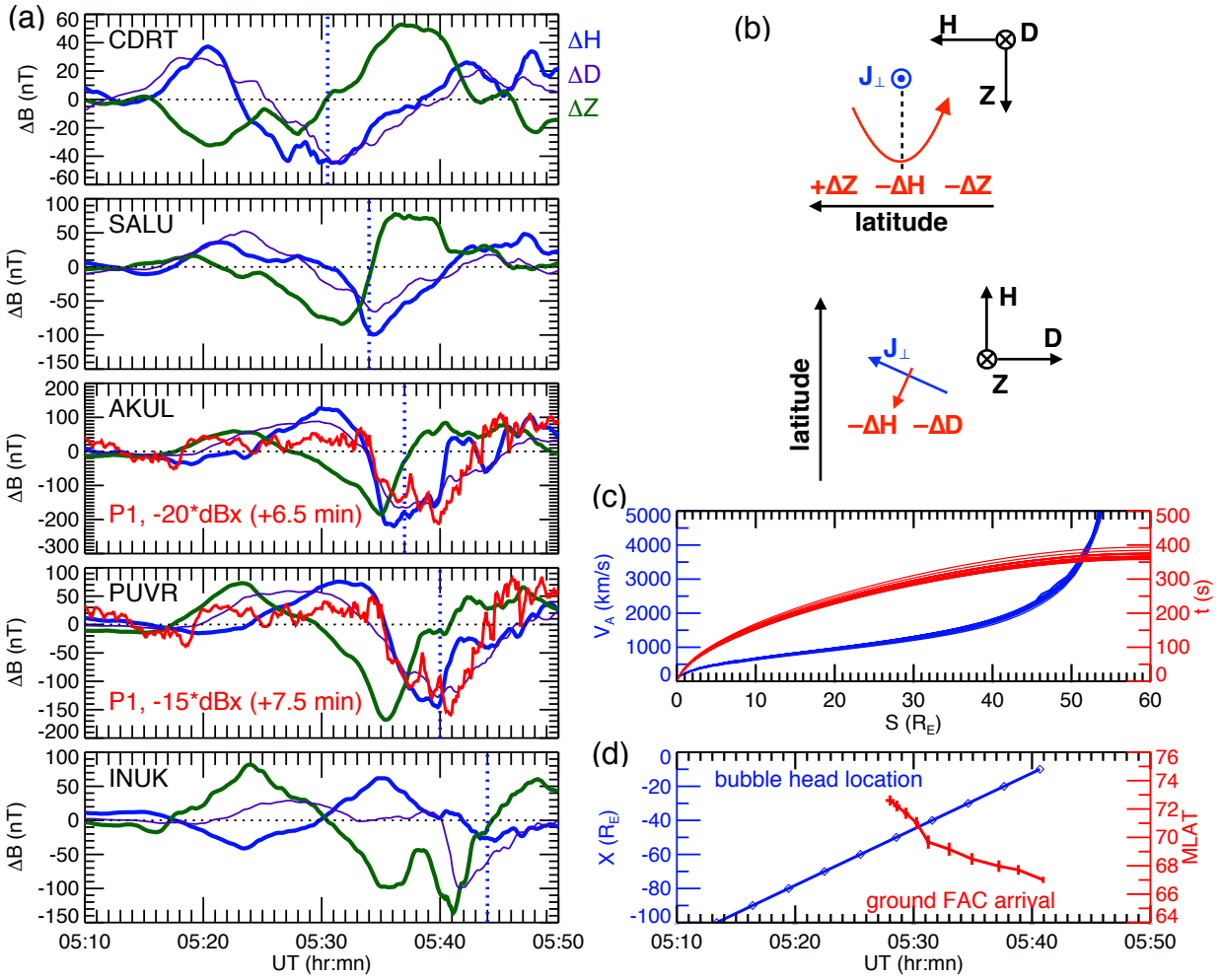

Figure 4. (a) Perturbations of the H, D, Z components of ground magnetometers. (b) Illustrations of ionosphere electrojet J⊥ (the blue arrows) and the associated ground perturbations (the red arrows). (c) Alfvén speeds and travel times as a function of field-aligned distances. (d) Predicted X-locations of the bubble front (blue) and ground arrival latitudes of FACs from the bubble front as a function of time.

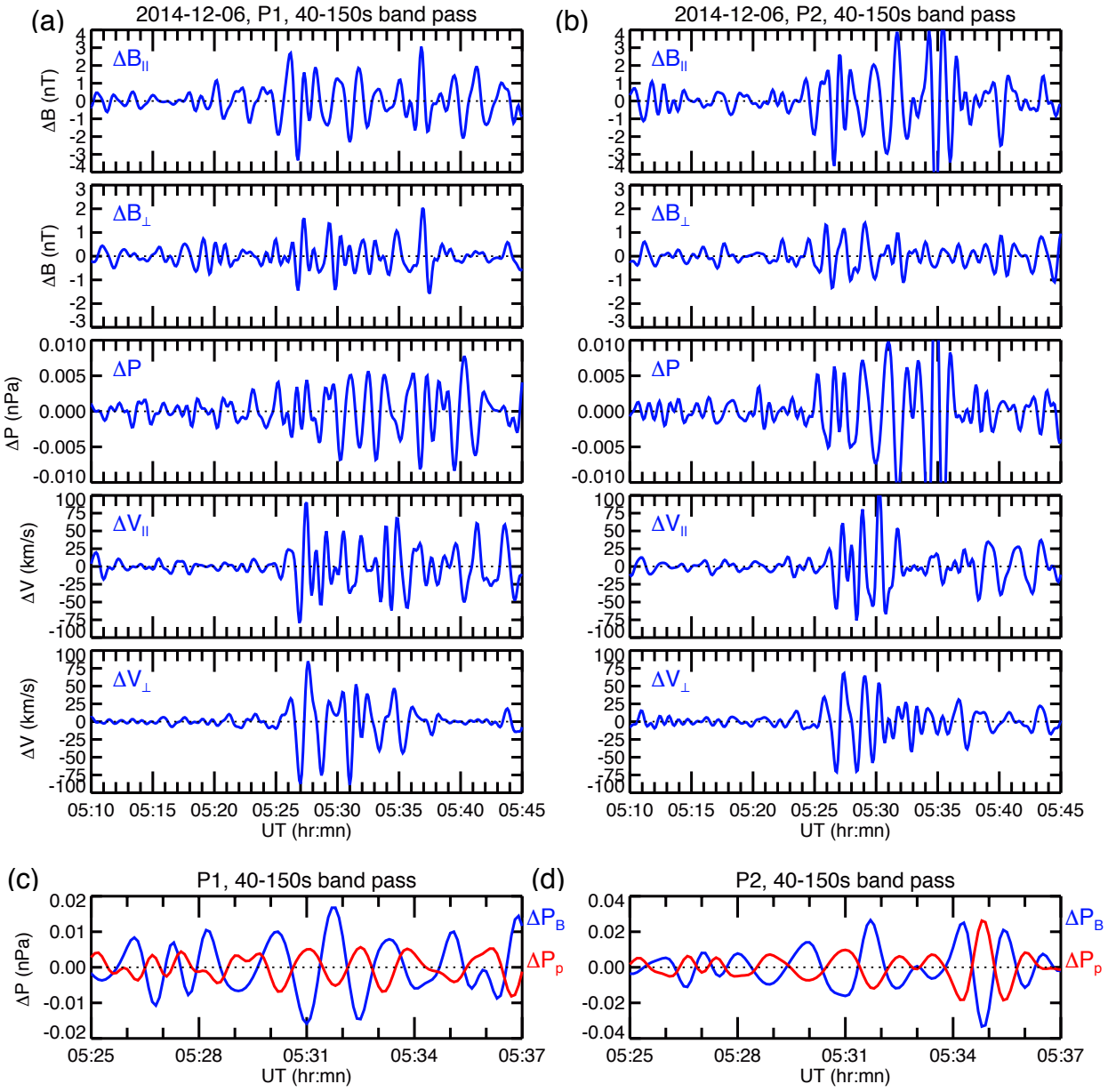

Figure 5. 40–150 s band-passed fluctuations of parallel and perpendicular magnetic field, plasma pressure, and parallel and perpendicular speed observed by (a) P1 and (b) P2. 40-150 s band-passed fluctuations of magnetic pressure (P_B) and plasma pressure (P_p) observed by (c) P1 and (d) P2.

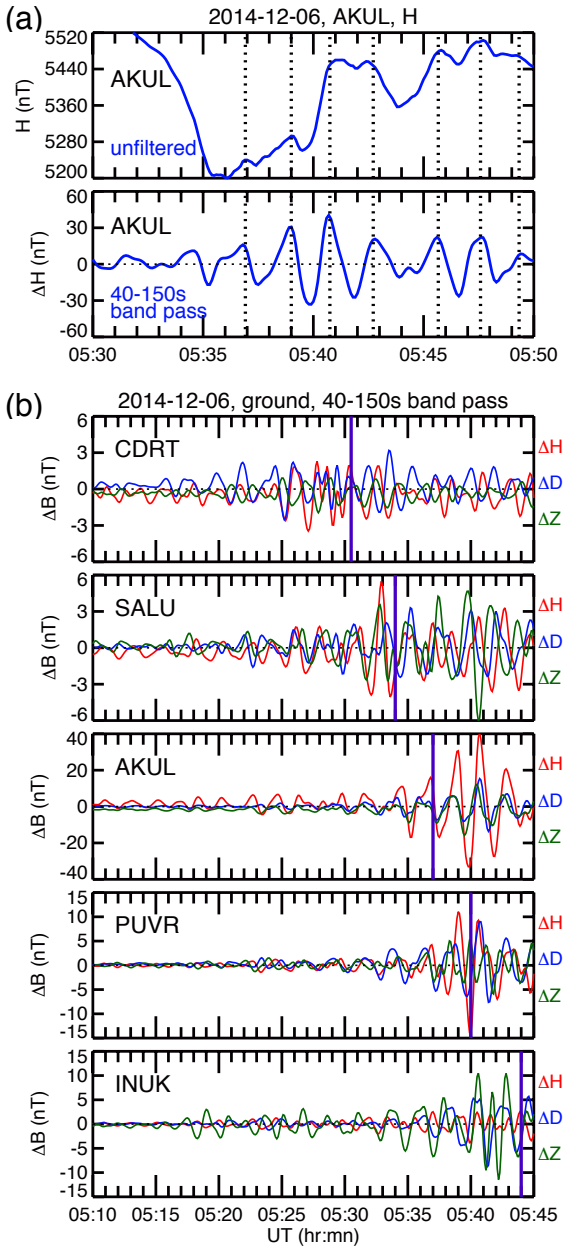

Figure 6. (a) Unfiltered (top) and 40-150 s band pass of H at AKUL station. (b) 40–150 s band-passed H, D, and Z components at different stations (the purple vertical lines indicate the minimum of ΔH).

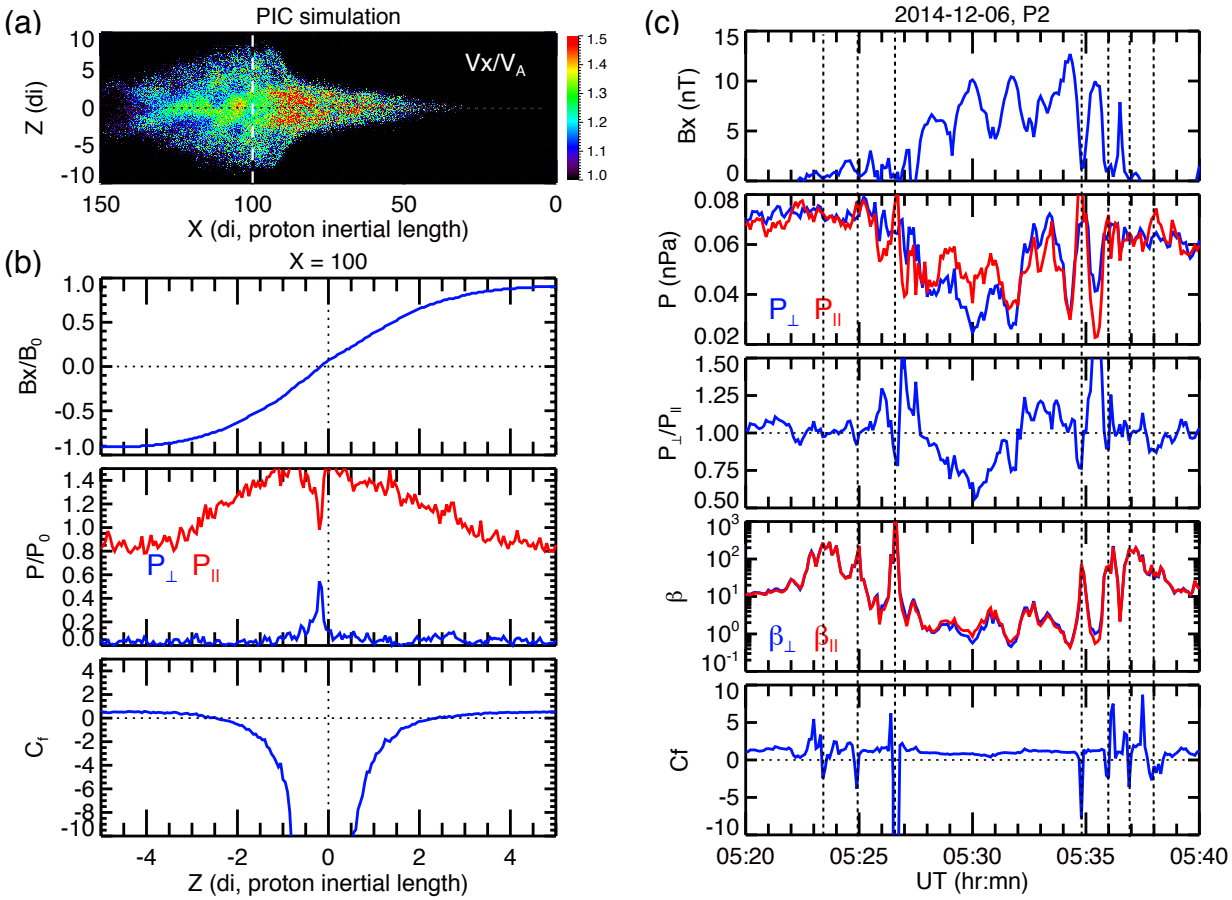

Figure 7. (a) Simulated Vx/V_A on the X-Z plane. V_A is Alfvén speed. (b) Simulated Bx, parallel and perpendicular plasma pressures, and C_f as a function of Z at X = 100. B_0 and P_0 are the initial values at the lobe (Z = 5). (c) Bx, plasma pressure, pressure anisotropy, plasma beta, and C_f observed by P1. The vertical black dashed lines indicate where $C_f < 0$.